Michael J. Evans, Paul R. Medwell, Zhiwei Sun, Alfonso Chinnici, Jingjing Ye, Qing N. Chan, Bassam B. Dally
**Downstream evolution of n-heptane/toluene flames in hot and vitiated coflows**
Combustion and Flame, 2019; 202:78-89



Published at: http://dx.doi.org/10.1016/j.combustflame.2019.01.008

# Downstream Evolution of *n*-Heptane/Toluene Flames in Hot and Vitiated Coflows

M.J. Evans[a,*], P.R. Medwell[a], Z. Sun[a], A. Chinnici[a], J. Ye[a,b], Q.N. Chan[c], B.B. Dally[a]

[a]*School of Mechanical Engineering, The University of Adelaide, Adelaide, SA 5005, Australia*
[b]*School of Aerospace, Mechanical and Mechatronic Engineering, The University of Sydney, NSW 2006, Australia*
[c]*School of Mechanical and Manufacturing Engineering, University of New South Wales, Sydney, NSW 2052, Australia*

**Abstract**

The scenario of fuel injected into hot surrounds is found in a range of practical combustion applications. These flame conditions have been emulated using a jet-in-hot-coflow-burner using prevaporised *n*-heptane and mixtures of *n*-heptane and toluene, relevant to gasoline and diesel fuel surrogates. This paper reports measurements of six lifted, turbulent flames, with a constant jet flow of a prevaporised fuel/$N_2$ mixture at 380 K into various hot and vitiated coflow conditions. Five of these flames issued into coflows generated by the combustion of different mixtures of ethylene/air and one had a coflow from a natural gas/air flame. Two *n*-heptane/toluene fuel blends were also measured to study the effect of soot propensity. Gas sampling, non-linear excitation regime two-line atomic fluorescence (NTLAF) and laser-induced incandescence (LII) were used to characterise the flames, investigate the mixing between the hot coflow and the surrounding air, and measure the flame temperature for the different coflow configurations. A comparison of results of the flames issuing into hot coflows is presented, indicating that the hottest flame is not associated with the coflow containing the highest concentration of $O_2$, but with the minimum soot loading and, consequently, the minimum radiative heat loss. Subsequent numerical simulations of canonical opposed-flow flames demonstrate that the soot loading in the downstream region of the flames is strongly dependent on PAH formation in the hot coflow region and further analyses reveal the chemical pathways which are most impacted by small variations in hot coflow composition.

*Keywords:* Heptane, Toluene, Turbulent Flames, Vitiated Coflows, MILD Combustion

## 1. Introduction

Flames issuing into hot and vitiated environments are found in practical combustion applications such as gas turbines, furnaces and other devices featuring strong exhaust gas recirculation (EGR), e.g. homogeneous charge compression ignition (HCCI) engines. These environments may be emulated in laboratory-scale research burners by the use of the jet-in-hot-coflow (JHC) configuration, where a jet of fuel issues into a coflow of combustion products [1–4]. This JHC burner is similar to the vitiated coflow burner (VCB) [5–8]. Both configurations have previously been used to measure soot-free regions in hydrocarbon flames [1, 2, 6, 7, 9] or to investigate flame stabilisation in the coflow-controlled region of a jet burner [7–12]. These studies have not, however, been able to provide detailed, downstream measurements of non-premixed jet flames in regions of significant soot loading due to interference on the optical diagnostic techniques that were used [13]. The fuel emanating from the central jet in this burner configuration may be in a gaseous form [1–3, 6–10, 14–19], atomised sprays [20, 21], or as liquid droplets [22–24] or solid particles in a carrier gas [25, 26]. The non-gaseous phase in such configurations, however, may also prevent the use of common, scattering-based, optical diagnostic techniques for temperature measurements [1, 2, 6, 7, 17, 18].

The ignition and structure of flames in hot and diluted coflows have been studied extensively in the context of lifted flames [3, 4, 8, 12] and moderate or intense low oxygen dilution (MILD) combustion [1, 3, 4, 27]. This configuration features a central jet emanating into a hot coflow of combustion products, emulating the effects of EGR [28–30] or staged combustion in gas turbines [31], such as those using inter-turbine burners [32, 33]. Studies of these flames have often focused on the near-field, coflow-controlled, region of these flames [3]. This limited region of interest has arisen because of the focus on flame stabilisation mechanisms.

*Corresponding author. *Phone:* +61 8 8313 5460
*Email address:* m.evans@adelaide.edu.au (M.J. Evans)

Although detailed temperature and species data have been collected in the soot-free region of a range of flames under MILD combustion conditions [1, 2, 9] these data-sets have used scattering-based diagnostic techniques, and therefore cannot be applied to sooting or spray flames. Moreover, whilst these data have been used extensively for model validation, the boundary conditions of the burners have often not been fully characterised.

Turbulent flames stabilised in hot and vitiated coflows have been the subject of numerous previous studies investigating flame structure and stability [4, 6, 12, 14, 34, 35]. Of these and similar studies, global features, such as temperature, have been studied in and beyond the coflow- or pilot-controlled region of the jet flame [1, 2, 4, 9, 14, 22–24, 34–39]. These measurements in JHC burners demonstrate the persistent effect of the coflow stream beyond the coflow-controlled region. Whilst pointwise temperature measurements have previously been taken in this region [15, 16], visual observations of sooting propensities indicate that $C_2H_4$ flames stabilised on a hot coflow containing only 3% $O_2$ result in significantly less downstream soot than those in coflows with $O_2$ concentrations of 9%. Furthermore, $C_2H_4$ flames with 1:3 air dilution may be soot-free for more than 300 mm in coflows with 3% $O_2$, but the increased $O_2$ concentration results in soot-formation 125 mm from the jet exit plane [9]. In both cases, the coflow temperature and H/C ratio were held constant and the oxidant stream 300 mm downstream of the jet exit plane would mostly be composed of quiescent air. Despite this, the very different flame features indicate the lasting influence of coflow composition, suggesting a chemical effect which persists into the far downstream region of the turbulent flame brush and tip. In contrast to the sparse availability of the downstream effects of hot and vitiated coflows, numerous studies have been undertaken in piloted turbulent flames [12, 34–39], where the pilot may account for 1-12% of the total heat release [37, 38]. Investigations within these studies have shown that the pilot flames have negligible effects on global, far downstream structure of turbulent flames [36–39].

Two key components of primary reference fuels (PRFs) and gasoline/diesel surrogates are *n*-heptane (*n*-$C_7H_{16}$) and toluene ($C_7H_8$) [3, 40–49]. These fuels have been studied in isolation [3, 48, 49], in binary blends [42] and as two components in ternary and quaternary gasoline surrogates [43–47, 50]. Whilst the majority of these studies have focussed on fuel

surrogate development or ignition delay measurements, limited studies of these fuels in canonical diffusion-flame burners are presently available [40].

Previous investigations of $n$-heptane in hot and oxygen-diluted environments have demonstrated significantly different behaviour to lower hydrocarbon fuels, which has been attributed to its multiple fuel pyrolysis/decomposition pathways [3]. The combination of different ignition pathways, and a distinct region of negative net heat release with highly diluted (3% $O_2$ vol./vol.) hot oxidants [3], warrants the further investigation of $n$-heptane, and its blends, as a surrogate for more complex, practical fuels.

A well-known feature of $n$-heptane ignition is the negative temperature coefficient (NTC) behaviour, occurring between 650-850 K at atmospheric pressure [51]. This range shifts to higher temperatures with increasing pressure [45, 51], such as in HCCI engines, resulting in a significant effect on ignition delay times and flame stabilisation mechanisms [40]. Whilst NTC behaviour is not present in toluene combustion, previous studies have shown that a 1:1 $n$-heptane/toluene mixture features an NTC region, although the low-temperature ignition process is delayed relative to pure $n$-heptane [46]. This addition of toluene, in turn, increases the octane number of the fuel blend [46]. Although these studies have performed in-depth kinetics analyses of ignition processes, they have not considered the increased prevalence of soot formation due to toluene addition, and its subsequent effects on flame temperature.

This work explores the behaviour of $n$-heptane and $n$-heptane/toluene flames under different hot and vitiated coflow conditions. Initially, the study investigates the downstream differences of $n$-heptane flames resulting from different coflow streams before investigating the effects of fuel blends. This work, similar to previous studies [3], focuses on prevaporised liquid fuels to eliminate the complex mechanism of droplet evaporation, and provides comparative data for future spray-flame studies. Unlike previous work, however, temperature and soot volume fraction are measured beyond the coflow-controlled region. Additionally, the persistence and mixing of the coflow stream and quiescent air are reported, which aid interpretation of the NTLAF results and will be beneficial for future modelling of these flames.

## 2. Methodology

### *2.1. Burner Description and Flame Cases*

Experiments were undertaken in flames stabilised on a JHC burner [52] similar to that used in previous studies [1, 3, 9]. The burner features a 4.6 mm I.D. (6.35 mm O.D., tapered over 4 mm to an O.D. of 5.2 mm at the jet exit plane) central jet which protrudes 25 mm above a 110 mm I.D. porous bed burner, producing an annular coflow of hot combustion products. The total length of the central pipe was more than 100 times its diameter to ensure fully-developed flow at the jet exit plane. The porous bed burner was surrounded by a secondary annular coflow (130 mm I.D.) of air at approximately 0.4 m/s to reduce fluctuations downstream caused by the mixing of the hot coflow and quiescent room air (at approximately 21°C).

The fuel jet stream issuing from the central jet contained 35% prevaporised fuel (by mass), in an $N_2$ carrier gas. The fuel mixtures studied were pure *n*-heptane (termed HEP), 1:3 *n*-heptane/toluene, and 3:1 *n*-heptane/toluene blends (termed H25 and H75 respectively). These volumetric ratios describe the fuel mixtures in their liquid state at room temperature. The bulk mean Reynolds number at the jet exit was fixed at 10,000. The fuel was diluted with $N_2$ and heated using a controlled evaporated mixer (CEM), and exited the jet at a temperature of 380 K to ensure completely prevaporised fuel. Approximately 10% of the total volumetric flow (equal to approximately 4 nLpm) of $N_2$ in the jet bypassed the CEM to carry indium nano- and micro-particles produced by means of ablation [53–55]. The CEM and seeded streams were recombined in a heated pipe upstream of the burner assembly.

Four different coflow conditions are investigated in this study: three from the combustion of ethylene/air (cases HEP-1 – HEP-3) and one from a natural gas/air flame (HEP-4). The coflows termed HEP-1 – HEP-3 were selected to target a range of temperatures and $O_2$ concentrations, while the HEP-4 case provided an additional variation in the $CO_2/H_2O$ ratio. The bulk velocities of the hot coflow streams just upstream of the jet exit plane were held at 1.1 m/s in all cases. The coflow conditions are summarised in Table 1, which include

the calculated equilibrium molar concentration of oxygen ($X_{O_2}$), carbon dioxide ($X_{CO_2}$) and water vapour ($X_{H_2O}$) in the coflow, as well as the measured temperature ($T_{cofl}$).

The different compositions and temperatures of each coflow described in Table 1 result in slight differences in properties such as density and viscosity. Although these differences are, in themselves, small (e.g. coflow densities are expected to be differ by no more than 7%) they may result in slight differences in the mixing between the hot coflow, fuel-jet and air streams. These variations, however, may be compounded by the range of $O_2$ concentrations in the HEP-1 – HEP-4 cases, and different ignition properties of the *n*-heptane/toluene blends, which affect the temperature and structure of the turbulent flame-sheet. This introduces an additional level of complexity to the cases investigated in this study. Such systems are, however, analogous to practical systems involving secondary combustion stages and dilution air, such as aero-engines, and the magnitude of the impact slight changes in the hot coflow have on the downstream flame are still yet to be fully understood.

The inclusion of the outer air-coflow lessens the impact of variations in the hot coflow and fuel streams, as a hot coflow large enough to ensure a two-stream problem along the entire length of the flame reacts is not practicable and confinement would introduce the further complication of flame-wall interactions. Diagnostics were not available to simultaneously quantify the temperature field, fuel and $O_2$ concentrations, following soot inception.

[Table 1 about here.]

### *2.2. Experimental Techniques*

Planar thermography was performed using non-linear excitation regime two-line atomic fluorescence (NTLAF) of indium [24, 49, 54, 56–58]. Soot volume fraction was measured using the laser-induced fluorescence (LII) technique [52, 55, 59–63]. The optical set-up was similar to previous studies, with more detail presented in [49, 52, 55, 63]. This NTLAF thermography technique has previously been successfully applied in sooting flames [13, 52, 54, 55, 57, 58, 63, 64], and the effects of soot loading have been assessed quantitatively [13, 57, 58, 64].

Thermography through NTLAF is performed on atomic indium seeded into the fuel stream by laser ablation [65]. The energy of the focused 532 nm ablation laser was ~0.1 J/pulse, similar to previous studies using the same apparatus [66]. Laser sheets with wavelengths tuned to the indium transitions at 410.18 nm and 451.13 nm were produced by two dye lasers, and used to pump the ground and thermally excited states (with electronic energy difference $\Delta E_{10}$) of atomic indium. Laser energies were approximately 6 and 0.6 mJ/pulse, respectively. A total of 500 image pairs of Stokes and Anti-Stokes signals were recorded using a single f-number 1.2 lens through a custom-made dichroic beam-splitter arrangement onto two ICCD cameras with gate widths of 40 ns. Both the Stokes and Anti-Stokes signal were collected through narrowband (1.2 nm FWHM) to minimise prompt LII signal and any scattering from the incident laser beam. Additionally, undesired interaction between other lasers in the pulse train and the soot particles were assessed independently, under the highest soot loadings, and resulted in negligible interference. Raw images were smoothed with a 3×3 median filter before image matching and temperature quantification. After image matching, the spatial resolution is 150 $\mu$m/pixel in the region of interest, which is less than the sheet thicknesses of approximately 400 $\mu$m, which limits the actual optical resolution. The relative strengths of the Stokes and Anti-Stokes signals, $F_{21}$ and $F_{20}$ respectively, are used to determine the local gas-phase temperature, T, through (1):

$$T = \frac{\Delta E_{10}/k}{\ln\left(F_{21}\left(1+\frac{C_S}{I_{20}}\right)\right) - \ln\left(F_{20}\left(1+\frac{C_A}{I_{21}}\right)\right) + C_T} \tag{1}$$

In (1), $I_{20}$ and $I_{21}$ are the energy of the incident Stokes and Anti-Stokes laser beams, $k$ is the Boltzmann constant, and $C_A$, $C_S$ and $C_T$ are constants determined through daily experimental calibration. This technique is valid for estimating conditional temperature, $\langle T \rangle$, in fuel-rich mixtures with a single-shot accuracy within 100 K, between 800-2500 K [54]. The technique is not accurate below this temperature range owing to the low population density of thermally excited indium, which is probed using the Anti-Stokes beam, or in the fuel-lean reaction zone where atomic indium is oxidised [54]. Finally, it should be noted that

as the Stokes signal originates from atomic indium in its ground state, this signal may be used as a surrogate for imaging rich mixtures in the flow.

Soot volume fraction (SVF) was measured with LII using the experimental methodology described in detail elsewhere [52, 62, 63]. The fundamental output from an Nd:YAG laser with energy of 600 mJ/pulse was used to heat the soot particles, with prompt incandescence detected by an ICCD camera through an f-number 1.4 lens and a gate width of 40 ns [52, 55, 63]. This technique allows for the detection of soot with a minimum primary particle diameter of approximately 5 nm [63].

Laser sheets were nominally 20 mm high, however, only the central 15 mm are presented herein as planar images. Data were collected at ten downstream measurement locations for each case. The height of sheet centres ranged from 15 mm to 330 mm (spanning a total range of $x/D$ from 2 to 72) above the jet exit plane (also referred to herein as height above burner, HAB) to capture the temperature field from the flame base to the broadest part of the flame. Histograms were constructed at several locations in the flame (provided later in Table 2), with data taken from a 2 mm high strip centred at the nominal height. All flames were approximately 500 mm long.

The coflow temperature for all cases and downstream jet centreline profile of HEP-2 case were measured with an R-type thermocouple with a 175-$\mu$m-diameter bead, corrected for radiative heat transfer. Gaseous $O_2$ and $CO_2$ were measured (on a dry basis) using a calibrated gas analyser sampled through a 3.2 mm O.D., 1.6 mm I.D. probe, with a length of 80 mm normal to the flow bulk velocity. The probe diameter was kept as small as possible in order to minimise the disturbance of the flow-field. Quenching of the products is not necessary because they are at equilibrium conditions at the coflow exit plane. The estimated absolute accuracy of the gas analyser (based on calibration) is $\pm 0.1\%$ for $O_2$ and $\pm 0.2\%$ for $CO_2$.

### *2.3. Numerical Analyses*

Numerical analyses of steady-state, axisymmetric opposed-flow flames were undertaken using the OPPDIF solver in ANSYS Chemkin Pro. The one-dimensional analyses used

a mixture-averaged transport treatment of species, including the Soret effect. Gas phase radiation to ambient surroundings was neglected, however this has previously been shown to be negligible in the hot-coflow-controlled region of similar ethylene flames in a JHC burner [67]. Hence, the exclusion of radiation is not expected to significantly affect the kinetics or the phenomena discussed in this work.

A reduced mechanism for $n$-heptane and toluene combustion, consisting of 335 chemical species and 1610 reactions [47], was used for all simulations. This mechanism was reduced by Cai and Pitsch [47] from a comprehensive 1027 species, 8472 reaction PRF mechanism, published by Curran *et al.* [68]. The reduced, 355 species mechanism includes PAH with up to four aromatic rings (pyrene) and the analyses of aromatics follows a similar approach to recent work [52, 69]. This reduced mechanism has been successfully compared to the full mechanism and validated [47] against an extensive experimental dataset for various fuel blends with $n$-heptane and toluene [43, 50, 70–80].

As per the experimental cases, the fuel stream was diluted with 65% $N_2$ by mass and oxidant compositions and temperatures were taken from Table 1. Velocities were set such that both streams had an equal momentum and an average normal strain rate $\sim$50 $s^{-1}$. This canonical opposed-flow configuration has previously been used to analyse the chemical structures of both laminar and turbulent diffusion flames under a wide range of conditions [1, 5, 7, 11, 14, 16, 18, 52, 56, 81–88].

## 3. Results and Discussion

### *3.1. Mean Flow-Field and Boundary Conditions*

The measured mean values of $O_2$ and $CO_2$ mole fractions, for case HEP-2, at the centre plane region above the jet, are presented in Fig. 1. Data were collected at 15 radial locations spanning a total of 100 mm: the centreline, then every 5 mm until 20 mm, followed by every 10 mm until 50 mm either side of the centreline; at 5 heights including the jet exit plane up to 85 mm downstream. The central, hatched, regions of the species fields represent the fuel stream where gas concentrations could not be measured due to the high concentration of pre-vaporised liquid fuel. These results suggest that the limit to which flame may be considered

coflow-controlled is approximately 70 mm downstream of the jet exit plane. Further downstream, mixing between the jet, annular air and hot coflow streams is evident by elevated $O_2$ and reduced $CO_2$ concentrations adjacent to the flame. The flame, in turn, is indicated by regions of very low mean $O_2$ and peak mean $CO_2$ concentrations at this height. The apparent discrepancies between the dry-basis measurements and the values in Table 1 are due to the calculation of equilibrium species on a wet-basis. The values, however, agree to within the the measurement accuracy of the gas analyser, following conversion to dry-basis.

Similar to the $CO_2$ and $O_2$ fields, the temperature field outside of the flame is expected to transition from the measured hot coflow value to that of room air due to three-stream mixing. Differences observed far downstream in flames with identical jet compositions but stabilised on different coflows, are consequently expected to be the persistent effects of the hot coflow on the upstream turbulent flames rather than due to variations in the local oxidant composition.

[Fig. 1 about here.]

The measured coflow temperature for HEP-2 is shown in Fig. 2. The radial temperature profile at the jet exit plane shows a maximum difference of less than 10 K at equal radial locations, within 30 mm of the centre of the burner. Temperature distributions for the other coflows were similarly uniformly distributed and axisymmetric (not shown).

[Fig. 2 about here.]

Understanding the extent and shape of the mixing field is critical to interpret the results of the flame appearance and laser-based NTLAF (among other) diagnostics. Without knowledge of the mixing field, the properties of the oxidant cannot be determined locally at the flame front and conclusions drawn about flame behaviour or structure may be erroneously attributed to the hot coflow. Therefore, the mixing between the fuel stream, hot coflow stream, annular air stream and surrounding quiescent air must both be understood for interpretation of measured data, particularly far downstream of the jet exit plane, and well-characterised for thorough model validation [89, 90]. Although some data for these

fields are already available from previous data-sets of flames in hot coflows studied using scattering techniques [1, 3, 6, 8, 12], the three-stream mixing cannot be measured using NTLAF (as the conditions are both cool and lean). The data presented in Figs. 1a and 1b may be used to provide verification for modelling the three-stream mixing effects in JHC burners using computational fluid dynamics, facilitating more accurate understanding of the fundamental combustion processes.

### *3.2. NTLAF Measurements of n-Heptane Flames*

Instantaneous measurements of the temperature field of all four pure $n$-heptane flames were centred at heights ranging from 15 mm to 330 mm above the jet exit plane. The mean lift-off heights of the flames were all approximately 10 mm, although lift-off height increased slightly with decreasing coflow $O_2$ concentration. Photographs of all flames are shown in Fig. 3, showing the delayed onset of soot formation with decreasing $O_2$ in the coflow of the $n$-heptane flames, as well as $n$-heptane/toluene flames (which are discussed in more depth in §3.3 and 3.4). Lift-off heights were defined as the location where gas temperatures reached 800 K in the averaged, conditional temperature fields. Images centred at 15 mm above the jet exit plane (not shown for brevity) show isolated pockets of high temperatures, suggesting the presence of ignition kernels, upstream of lifted flame bases. This mechanism of flame stabilisation is typical of autoignitive turbulent flames [11], and is consistent with previous conclusions of prevaporised $n$-heptane flame stabilisation in hot and diluted coflows [3]. The lift-off heights of each flame are summarised in Table 2, along with the most probable temperature centred about three different heights. Probability density functions (PDFs) obtained from the ensemble of images are provided in Fig. 4. Noticeably, the flame in the HEP-4 case is the hottest at both 62.5 mm downstream of the jet exit plane and 317.5 mm downstream, despite the coflow having the lowest $O_2$ concentration.

[Table 2 about here.]

[Fig. 3 about here.]

Comparison between PDFs of temperature in the histograms in Fig. 4, with modal values presented in Table 2, demonstrates that the HEP-4 flame is hotter than the HEP-1 flame (which, in turn, is of a similar temperature to cases HEP-2 and 3), despite having 3% less available $O_2$ (vol./vol.) in the coflow stream. This trend is consistent across all heights. As both coflows in cases HEP-1 and 4 are held at similar temperatures, this can be associated with the influence of the coflow $CO_2/H_2O$ ratio on *n*-heptane combustion through chemical or physical effects. This is consistent with simulations of laminar $C_2H_4$ flames with hot coflows where coflows with higher ratios of $H_2O$ to $CO_2$ exhibited hotter flame fronts, particularly under MILD conditions [87, 91–95].

[Fig. 4 about here.]

[Table 3 about here.]

Initial mixing between the coflow and quiescent air occurs at ∼70 mm above the jet exit plane (see Fig. 1). At, and beyond this point, the flame is no longer strictly coflow-controlled, with entrainment from the outer air coflow and ambient room air with both oxidant streams having an effect on the flame. At, and beyond, this height, the HEP-1 and HEP-4 flames begin to exhibit intermittent 'ruptures' in the flame front. This is in contrast to unbroken flame fronts consistently observed at 60 mm above the jet exit plane. A typical rupture is shown in Fig. 5. The frequencies of these ruptures was determined manually and are given in Table 3, centred at several heights. These ruptures appear on both sides of the jet exit plane with similar frequency, but are only seen to occur on both sides simultaneously in a comparatively small number of frames (∼1% of frames). Of all the cases in this study, HEP-4 demonstrates the greatest propensity for ruptures in the flame sheet at any height. This is consistent with HEP-4 also demonstrating the greatest lift-off height in the coflow-controlled region. This trend is consistent with the trend in coflow $O_2$ concentration—and hence mixture reactivity—between these two cases, although in contrast to the trends in flame temperature, suggesting a different underlying cause of the temperature discrepancy. The frequency of ruptures is similar in cases HEP-2 and 3, whilst HEP-1 has the least number of observed discontinuities in the flame sheet at any given height.

Ruptures in the conditional temperature field may be indicative of relatively low temperatures (T<800 K, below the minimum measurable temperature for indium NTLAF) or the absence of atomic indium. In the case of the former, ruptures would correspond to an absence of thermally-excited anti-Stokes signal, however, the ground-state Stokes signal would still be measured. A typical comparison between the conditional temperature, Stokes signal and Anti-Stokes signal is therefore presented in Fig. 5, showing a rupture centred at 110 mm downstream of the jet exit plane. The absence of Stokes signal in Fig. 5 indicates that these ruptures are evidence of an absence of atomic indium. Possible reasons for the absence of atomic indium are:

1. all free indium atoms have been oxidised [57, 96],
2. entrainment of gas that originates from the unseeded oxidant stream, diluting the atomic indium to below measurable levels, and/or
3. gases are not hot enough to decompose the seeded indium into atomic indium.

In general, all three mechanisms may be active at the boundary between the flame and ambient cool air. It is, however, unlikely that all free indium has been oxidised at this height, as demonstrated by the reliable signal further downstream in conjunction with similar studies of turbulent toluene [52], $C_2H_4$ [54] and $CH_4$-based [55] flames using a comparable method of seeding indium micro- and nanoparticles. Such particles would continue to readily release atomic indium into the flame preheat zone [66], which would be detectable in the image of the Stokes signal. Such a preheat zone is not observable from the Stokes signal, however, suggesting the absence of a flame front coinciding with the rupture shown in Fig. 5. The two other aforementioned mechanisms are suggestive of cool, quiescent air or cool fuel at the location of the rupture, however identification of the local composition and conserved scalar dissipation rates to support a more in-depth analysis of the ruptures are not possible using the NTLAF technique used in this study and would require further investigation.

[Fig. 5 about here.]

Measurements centred at 165 mm downstream of the jet exit plane demonstrate a significantly reduced propensity for ruptures than at 110 mm downstream (see Table 3). This

is a result of the increasing local $O_2$ concentration, as well as reduced local strain-rates and hence longer fluidic time-scales, due to lower velocities owing to jet decay. There is little change in the most probable conditional temperature in cases HEP-1 to HEP-3, although the modal conditional temperature in HEP-4 slightly increases. This is despite HEP-4 still having the greatest propensity for rupturing. These results further demonstrate the persistent effect of coflow composition on downstream flame temperature, with the hottest flame—HEP-4—stabilised in the coflow with the lowest concentration of $O_2$. Interestingly, HEP-4 has a similar coflow temperature to HEP-1, which has the highest coflow $O_2$ concentration but the lowest downstream flame temperatures. Both cases have similar concentrations of coflow $CO_2$, however HEP-4 has nearly twice the molar concentration of gaseous $H_2O$ in the hot coflow. These differences, in themselves, cannot account for the higher temperature in HEP-4, particularly beyond the coflow-controlled region of the flame, prompting further analyses presented in §3.5.

### *3.3. NTLAF Measurements of n-Heptane/Toluene Flames*

Toluene and *n*-heptane are both hydrocarbons with seven carbon atoms, but with eight and sixteen hydrogen atoms, respectively. Accordingly, there is less than a 10% difference between the molecular masses of the two molecules. With these similarities, blending toluene and *n*-heptane in the fuel stream approximately maintains the concentration of the atomic carbon in the flame. Because of this, the adiabatic flame temperatures of these blends differ very little, however, the aromatic structure of toluene results in a significantly increased propensity for soot formation. Comparisons of measured gas temperatures in the H25-2 and H75-2 flames (see Table 1 for details) are shown in Fig. 6. Data were taken from the same downstream locations as previously presented in Fig. 4, and are additionally summarised in Table 4.

[Table 4 about here.]

[Fig. 6 about here.]

Analyses of the temperature PDFs for the H25-2 and H75-2 flame demonstrates that an increase in the toluene concentration in the fuel stream leads to a reduction in flame temperature by 150 – 200 K, at 317.5 mm above the jet exit plane, well downstream of the coflow-controlled region. Similarly, the temperatures of the H25-2 flame are slightly less than those in the HEP-2 flame in the coflow-controlled region (recall Table 4). The differences between flame temperatures are consistent between cases and across the different heights in Table 4. Differences in temperature are even more significant further downstream of the jet exit plane. The significant differences between flames with varying concentrations of toluene are in spite of the similar adiabatic flame temperatures for the different fuel streams. This suggests that the discrepancies may have a different underlying cause beyond gas-phase combustion chemistry.

### *3.4. Soot Volume Fraction in n-Heptane/Toluene Flames*

The molecular structure of toluene can be described as an aromatic ring of six carbon atoms with the addition of a methyl group. This structure is subsequently prone to polyaromatic hydrocarbon (PAH) formation [97, 98] and, hence, soot particle production. This is demonstrated in Fig. 3 where increases in soot loading are evident along the entire length of the flame with increasing toluene concentration. Noticeably, visible soot is present within ∼45 mm of the jet exit plane in case H75-2, and within ∼20 mm for case H25-2, following the addition of toluene to the fuel stream.

Blending toluene and *n*-heptane fuels has a significant impact on the total soot loading of the flame, which is evident from Fig. 7. This figure shows the total soot loading (in volume fraction), at different heights in the flame. This value was calculated by integrating along the radial position, and integrating azimuthally along each row of pixels in the 2 mm data strip in each image, and then averaged. This figure demonstrates that the addition of toluene to 25% of the liquid volume increases the soot loading by up to three orders of magnitude. This is apparent at 217.5 mm above the jet exit plane, where the addition of 25% toluene results in an increase in soot loading from ∼10 to ∼5000 ppm·mm$^3$. This effect is less extreme after further increasing the toluene volume to 75%.

The addition of toluene markedly accelerates the soot formation, with significant SVF in the hot and diluted coflow-controlled region. In both H25-2 and H75-2 cases, Fig. 7 shows that the peak value of integrated SVF occurs approximately 300 mm above the jet exit plane, whereas the peak integrated SVF was at, or beyond, the maximum measurement height in the HEP-2 flame. Noticeably, the soot visible in Fig. 3 at heights less than 50 mm above the jet exit plane, were not measurable using LII in this study. These SVF measurements may be reasonably well described using a power law fit (of the form $y = ax^b$) well upstream of the region of peak soot loading. Fits are shown in Fig. 7.

The addition of toluene to the fuel jet results in a significant reduction in flame temperature, as shown previously in Fig. 6 and Table 4. These differences in temperature are most significant beyond the coflow-controlled region. At a height of 112.5 mm above the jet exit plane, the temperature of the H25-2 flame is similar to that the H75-2 flame, however, by 167.5 mm above the jet exit plane, the H25-2 flame is cooler by approximately 200 K (recall Table 4). In stark contrast, the modal temperature of the HEP-2 flame increases by 50 K over the same distance. These differences can be related to the soot loading and thermal radiation.

The soot loading may be used to calculate the radiative heat losses from the flame. By assuming that the flame is optically thin, the radiation loss from the flame, $q_{loss}$ in W/m$^3$, can be approximated by:

$$q_{loss} = 3.337 \times 10^{-4} f_v T^5 \; + \; 4 k_P \sigma T^4 \tag{2}$$

from [99], where $k_P$ is the Planck mean absorption coefficient, and $\sigma$ is the Stefan-Boltzmann constant [99, 100]. This approach has been successfully applied to sooting, laminar ethylene [99, 101] and acetylene [100] flames, although radiative losses may be significantly enhanced with the effects of turbulence [102, 103]. As $\langle T \rangle$ was not measurable in all pixels with soot measurements, the radially integrated mean $q_{loss}$ was evaluated at each height using the modal value of $\langle T \rangle$ and the measured distribution of $f_v$. The value of $k_P$ was calculated using the modal temperature and the peak mole fractions of $CO_2$, CO, $H_2O$ and $CH_4$ determined

using opposed-flow flame calculations. Following this approach, the values of $q_{loss}$ from gas radiation are approximately constant along the length of the flame, and are tabulated in Table 5.

[Table 5 about here.]

The radially integrated radiative heat loss at different heights above the jet exit plane, can be separated into two components, namely radiative soot (Fig. 8) and gas (summarised in Table 5) emissions, expressed in W/mm along the axial length of the flame. It is pertinent to recall that the LII technique used in this study is only reliable for soot structures with $d_p \gtrsim 5$ nm, and hence radiation from smaller soot particles, expected closer to the jet exit plane [104] and evident from Fig. 3, cannot be estimated.

The plot in Fig. 8 shows an increase in heat loss with the inclusion of 25% toluene in H75-2 flame relative to the HEP-2 flame of up to several orders of magnitude. The radiative power loss from soot at the 217.5 mm height increases from ∼10 W/mm in the H75-2 case to ∼5000 W/mm in the H25-2 case. This is further increased in the H25-2 flame containing 75% toluene, although the difference is significantly less. This trend in heat loss with increasing toluene fraction is similar to the trend of increasing integrated soot loading seen in Fig. 7, approximately following a power law upstream of the region of peak soot loading. These radiative losses from soot emissions represent the dominant contribution to the total flame radiant fraction, and are several orders of magnitude greater than the heat losses from gas radiation (Table 5).

[Fig. 7 about here.]

[Fig. 8 about here.]

The results of opposed-flow analyses are provided in Fig. 9 to provide further insight on the effects of toluene blending with *n*-heptane. The plot shows the combined mass fraction of all PAH species (all species with two or more benzene rings, denoted as $Y_{A_{2+}}$), used as a surrogate for soot formation, similar to previous work [52]. The data in Fig. 9

demonstrate the linear increase in total PAH concentration for fuel mixtures with increasing concentrations of toluene. Although this trend is qualitatively similar to that in Fig. 7, the different quantitative trends may be the result of molecular growth beyond the kinetics mechanism used in this study [47], and the soot aggregation and agglomeration processes which are not considered in the modelling approach.

[Fig. 9 about here.]

Mass fractions of PAH were calculated for autoignitive flames near the transition to the MILD combustion regime [3]. This regime is well known for its low soot production [3, 4, 9, 17, 27, 85, 105–107]. As conditions approach MILD combustion, through elevated temperatures and decreasing local $O_2$ concentrations, the magnitude of negative heat release reduces [3, 17, 85, 105, 106]. This, in turn, reduces fuel pyrolysis and PAH formation relative to combustion with cold air. Consequently, the predictions of $Y_{A_{2+}}$ in Fig. 9 are expected to be conservative along the length of the flame, with the sooting propensity increasing downstream beyond the coflow-dominated region.

Increased PAH concentration is indicative of the increasing soot propensity due to toluene addition. This is consistent with the photographs shown in Fig 3. Although the increased concentration of soot in the coflow-controlled region of the flame appears to be evident in the photographs, and its formation is supported by the opposed-flame analysis, only limited concentrations of soot were measured in this region. Consequently, soot $f_v$ in this region is suspected to be below the minimum threshold of the configuration in this study. Nevertheless, the photographs provide evidence that the soot particles in this region still have an impact on radiative heat losses, which may account for the temperature differences presented in Table 4.

### *3.5. Soot Volume Fractions in n-Heptane Flames*

Comparison of the for all the HEP cases are presented in Fig. 10. This plot demonstrates that the total soot concentration increases with increasing $O_2$ concentration in the coflow. Soot volume fraction data were measurable in all cases from 217.5 mm (47D) above the jet

exit plane. It is noteworthy that the 1% difference in coflow $O_2$ between the HEP-2 and 3 cases resulted in an average 2.4-fold increase in soot concentration at heights greater than 250 mm above the jet exit plane, despite both cases having very similar coflow temperatures. Integrated SVF measurements for the *n*-heptane flames all showed good agreement with a fitted power law curve.

[Fig. 10 about here.]

The increased soot in HEP-2 relative to HEP-3 may explain the very similar flame temperatures between the two cases, despite HEP-2 having a slightly higher coflow $O_2$ concentration. The increased soot concentration in HEP-2 not only results in more radiant heat loss from soot particles, but the higher coflow $O_2$ concentration implies that the HEP-2 flame features fewer characteristics of the MILD combustion regime beyond the coflow-controlled region of the flame. Due to this difference, in the HEP-3 flame, the endothermic reactions typical of fuel decomposition are more significant than the exothermic combustion reactions [3, 85]. This not only results in slight reductions in flame temperature, but increases the propensity of forming small soot particles in the coflow-controlled region. This increase may explain the similarities in measured flame temperatures at all heights, despite HEP-2 having a slightly higher adiabatic flame temperature.

HEP-1 has the lowest coflow temperature, but the highest coflow $O_2$ concentration. In contrast, HEP-4 has the lowest concentration of coflow $O_2$ with a slightly higher (30 K) coflow temperature. HEP-4 is, therefore, closer to the MILD combustion regime than HEP-1. The reduced coflow $O_2$ concentration in HEP-4 suggests that the suppression of a negative heat release rate region is more likely in HEP-4, consistent with the reduced soot loading in HEP-4.

The discrepancy in total soot loading between cases HEP-1 and HEP-4 is more substantial at 47D above the jet exit plane than it is further downstream. At this height, the integrated SVF in HEP-1 is nearly two orders of magnitude greater than that in HEP-4. This difference decreases with downstream distance, reducing to a factor of four-and-a-half times

difference at 73D. This is despite the total integrated soot loadings increasing significantly between 47D and 73D in both cases.

The differences in total SVF lead to significant differences in radiant heat loss in the HEP flames. The contribution from soot is shown in Fig. 11, with losses due to radiation from gaseous $CO_2$, CO, $H_2O$ and $CH_4$ given previously in Table 5. As with the *n*-heptane/toluene flames, radiant heat loss from the *n*-heptane flames is dominated by soot. Figure 11 shows that the radiative heat losses from soot in HEP-1 are approximately threefold those in the HEP-4 flame. The results suggest that the hottest flame temperatures do not correspond to the greatest $O_2$ concentration in the coflow, but are closely tied to the propensity for soot formation, following similar power law curves. The formation of soot, however, appears to be closely related to the $O_2$ in the coflow, which is in agreement with previous studies on autoignitive and MILD combustion [1, 9, 85].

[Fig. 11 about here.]

The difference in soot loading in the HEP cases is supported by results from opposed-flow flame analyses. Following a similar approach to the *n*-heptane/toluene flames, Table 6 compares the calculated peak total PAH mass fraction for the four HEP cases. These data reveal a similar trend as seen experimentally with SVF, with the mass fraction of PAH increasing significantly with oxidant $O_2$ concentration. This suggests an increased propensity for soot, and hence, increased radiative heat loss from small soot ($d_p \lesssim 5$ nm) as was suggested for the *n*-heptane/toluene blends in §3.4.

Rate of production and sensitivity analyses were performed for naphthalene ($C_{10}H_8$, referred to herein as $A_2$) in the HEP-1 – HEP-4 cases. These analyses were undertaken at the minimum (most negative) net heat release rate where pyrolysis and, hence, soot precursor formation is prevalent. Analysis of the heat release rate profile indicates that peak PAH production, unsurprisingly, correlates with the most negative heat release rate, and confirms the phenomenological argument that this is less prevalent closer to the MILD combustion regime.

[Table 6 about here.]

Analyses of $A_2$ production (see Supplementary Data for additional figures for rate of production analyses and normalised sensitivity to reactions) demonstrates that the main pathway for $A_2$ production is, in all cases, from the reaction of the methyl radical ($CH_3$) with $C_9H_7$. Although this is the dominant formation reaction in each case, the absolute rate of production is maximum for HEP-1 and decreases with decreasing oxidant $O_2$ concentrations. Formation of $A_2$ through this reaction is increased by 5% from HEP-1 to HEP-2; decreased by 27% from HEP-1 to HEP-3 and decreased by nearly 70% from HEP-1 to HEP-4. The dominant means of $A_2$ consumption is, in all cases, via reaction with the H radical to form $C_{10}H_7$ + $H_2$, and this is most significant in the HEP-1 and HEP-2 cases. Additional reactions between $C_{10}H_7$ and H radicals produce further $A_2$, as do reactions between $C_6H_5$-$CH_2$ + $C_3H_3$ and $C_{10}H_7$-$CH_3$ + H.

Although the pathways which support $A_2$ production in the HEP cases are all common, the different oxidant compositions result in significantly different sensitivities to key reactions. In all cases, $A_2$ formation is inhibited by the recombination of $CH_3$ to $C_2H_6$, which is promoted under MILD combustion conditions [108] and this is, accordingly, most significant in the HEP-4 case. The relative sensitivity to this reaction is least significant in the HEP-2 case.

The significant reduction in $A_2$ between cases HEP-2 and HEP-3 is a result of reducing the $O_2$ concentration in the oxidant by 1%. This small decrease in the total oxygen results in a stronger sensitivity to the production of O and OH radicals from the reaction of H + $O_2$. The normalised sensitivity to this reaction is further increased in the HEP-4 case, where it is more influential than the recombination of $CH_3$ or the production of $C_2H_2$, with greater consumption of H corresponding to more $A_2$ production. This is due to the increased availability of H reacting with $A_2$ as well as $C_2H_4$, $C_2H_6$ and $C_3H_6$, which compete with the initial consumption of the *n*-heptane fuel and, hence, less $A_2$ and therefore soot.

## 4. Conclusions

Temperature fields of turbulent, autoignitive, lifted *n*-heptane/toluene flames issuing into hot and diluted coflows have been imaged using NTLAF thermography and prompt LII

for soot volume fraction. These data extend from the flame base region to over 330 mm downstream and are complemented by gas composition measurements of the mixing field between the fuel jet, hot coflow and air streams.

Thermography results using the NTLAF technique indicate that an $n$-heptane flame issuing into a natural gas/air coflow (case HEP-4) is hotter than those issuing into ethylene/air coflows (cases HEP-1 – HEP-3), despite higher $O_2$ concentrations in the coflow stream and similar, or higher, coflow temperatures. Flames of $n$-heptane/toluene fuel blends are similarly cooler than those with pure $n$-heptane. In both scenarios, this is attributed to significantly increased soot loading and radiant heat loss from soot, following examination of the LII measurements and simulated opposed-flow flames.

The results of the simultaneous conditional temperature and soot measurements, in conjunction with radiative modelling and chemical analyses, may be used to draw the following conclusions:

- The integrated soot loading dominates radiative heat losses in flames stabilised on hot and diluted coflows, but concentrations are significantly affected by the temperature and composition of the hot coflow.

- Small changes in coflow oxygen concentration result in significant differences in PAH formation, which translate to substantial differences in sooting propensity far downstream of the coflow-controlled region.

- Trends in temperature PDFs and modal temperatures within the coflow-controlled region persist far downstream into the flame brush, with downstream temperatures strongly coupled with soot loading.

- Increasing the proportion of toluene in binary mixtures of $n$-heptane/toluene fuels in hot oxidants results in an approximately linear increase in PAH production, resulting in up to three orders of magnitude increase in soot loading between pure $n$-heptane and a 3:1 $n$-heptane/toluene blend, and a further order of magnitude increase in total soot in a 1:3 mixture of $n$-heptane/toluene blend.

- Reducing oxidant $O_2$ concentrations in representative *n*-heptane opposed-flow flames results in a significant decrease in naphthalene ($A_2$) production as a result of H reacting with $C_2$ and $C_3$ species in preference to the fuel. This is compounded by enhanced recombination of $CH_3$ to form $C_2H_6$.

The results of this study provide quantitative insight into both the impact of soot loading on turbulent flame temperature, as well as the formation and persistent downstream effects of PAH species in jet flames stabilised on hot and vitiated coflows. These findings highlight the importance of the hot coflow on the global flame features, particularly the implications of small variations in ambient conditions on the chemical pathways in complex hydrocarbon combustion.

## Acknowledgements

The authors thank Mr Qian Li from Zhejiang University for his assistance in data collection. Financial support was provided by through the Australian Research Council (ARC) Discovery (DP and DECRA) grant scheme, and the United States Asian Office for Aerospace Research and Development (AOARD).

## References

[1] B. Dally, A. Karpetis, R. Barlow, Structure of turbulent non-premixed jet flames in a diluted hot coflow, Proc. Combust. Inst. 29 (2002) 1147–1154.

[2] P. R. Medwell, P. A. M. Kalt, B. B. Dally, Simultaneous imaging of OH, formaldehyde, and temperature of turbulent nonpremixed jet flames in a heated and diluted coflow, Combust. Flame 148 (1-2) (2007) 48–61.

[3] J. Ye, P. R. Medwell, M. J. Evans, B. B. Dally, Characteristics of turbulent n-heptane jet flames in a hot and diluted coflow, Combust. Flame 183 (2017) 330–342.

[4] A. A. Perpignan, A. G. Rao, D. J. Roekaerts, Flameless combustion and its potential towards gas turbines, Prog. Energy Combust. Sci. 69 (2018) 28–62.

[5] R. Cabra, T. Myhrvold, J. Chen, R. Dibble, A. Karpetis, R. Barlow, Simultaneous laser raman-rayleigh-lif measurements and numerical modeling results of a lifted turbulent $H_2/N_2$ jet flame in a vitiated coflow, Proc. Combust. Inst. 29 (2002) 1881–1888.

[6] R. Cabra, J.-Y. Chen, R. Dibble, A. Karpetis, R. Barlow, Lifted methane-air jet flames in a vitiated coflow, Combust. Flame 143 (4) (2005) 491–506.

[7] R. L. Gordon, A. R. Masri, E. Mastorakos, Simultaneous Rayleigh temperature, OH- and $CH_2O$-LIF imaging of methane jets in a vitiated coflow, Combust. Flame 155 (1-2) (2008) 181–195.

[8] A. Macfarlane, M. Dunn, M. Juddoo, A. Masri, Stabilisation of turbulent auto-igniting dimethyl ether jet flames issuing into a hot vitiated coflow, Proc. Combust. Inst. 36 (2) (2017) 1661–1668.

[9] P. R. Medwell, P. A. M. Kalt, B. B. Dally, Imaging of diluted turbulent ethylene flames stabilized on a Jet in Hot Coflow (JHC) burner, Combust. Flame 152 (2008) 100–113.

[10] A. Ramachandran, D. A. Tyler, P. K. Patel, V. Narayanaswamy, K. M. Lyons, Global Features of Flame Stabilization in Turbulent Non-premixed Jet Flames in Vitiated Coflow, 45th AIAA Fluid Dynamics Conference Paper AIAA 2015-2313.

[11] M. J. Evans, P. R. Medwell, H. Wu, A. Stagni, M. Ihme, Classification and Lift-Off Height Prediction of Non-Premixed MILD and Autoignitive Flames, Proc. Combust. Inst. 36 (3) (2016) 4297–4304.

[12] T. F. Guiberti, H. Cutcher, W. L. Roberts, A. R. Masri, Influence of Pilot Flame Parameters on the Stability of Turbulent Jet Flames, Energy Fuels 31 (3) (2017) 2128–2137.

[13] Q. Chan, P. Medwell, Z. Alwahabi, B. Dally, G. Nathan, Assessment of interferences to nonlinear two-line atomic fluorescence (NTLAF) in sooty flames, Appl. Phys. B 104 (1) (2011) 189–198.

[14] E. Oldenhof, M. J. Tummers, E. H. van Veen, D. J. E. M. Roekaerts, Ignition kernel formation and lift-off behaviour of jet-in-hot-coflow flames, Combust. Flame 157 (6) (2010) 1167–1178.

[15] E. Oldenhof, M. J. Tummers, E. H. van Veen, D. J. E. M. Roekaerts, Role of entrainment in the stabilisation of jet-in-hot-coflow flames, Combust. Flame 158 (8) (2011) 1553–1563.

[16] E. Oldenhof, M. J. Tummers, E. H. van Veen, D. J. E. M. Roekaerts, Transient response of the Delft jet-in-hot coflow flames, Combust. Flame 159 (2) (2012) 697–706.

[17] J. Ye, P. R. Medwell, B. B. Dally, M. J. Evans, The transition of ethanol flames from conventional to MILD combustion, Combust. Flame 171 (2016) 173–184.

[18] J. Ye, P. R. Medwell, K. Kleinheinz, M. J. Evans, B. B. Dally, H. G. Pitsch, Structural Differences of Ethanol and DME Jet Flames in a Hot Diluted Coflow, Combust. Flame 192 (2018) 473–494.

[19] A. R. Macfarlane, M. Dunn, M. Juddoo, A. Masri, The evolution of autoignition kernels in turbulent flames of dimethyl ether, Combust. Flame 197 (2018) 182–196.

[20] H. Correia Rodrigues, M. Tummers, E. van Veen, D. Roekaerts, Effects of coflow temperature and composition on ethanol spray flames in hot-diluted coflow, International Journal of Heat and Fluid Flow 51 (2015) 309–323.

[21] H. Correia Rodrigues, M. J. Tummers, E. H. van Veen, D. J. Roekaerts, Spray flame structure in conventional and hot-diluted combustion regime, Combust. Flame 162 (3) (2015) 759–773.

[22] W. O'Loughlin, A. Masri, A new burner for studying auto-ignition in turbulent dilute sprays, Combust. Flame 158 (8) (2011) 1577–1590.

[23] W. O'Loughlin, A. R. Masri, The Structure of the Auto-Ignition Region of Turbulent Dilute Methanol Sprays Issuing in a Vitiated Co-flow, Flow, Turbul. Combust. 89 (1) (2012) 13–35.

[24] P. R. Medwell, A. R. Masri, P. X. Pham, B. B. Dally, G. J. Nathan, Temperature imaging of turbulent dilute spray flames using two-line atomic fluorescence, Exp. Fluids 55 (11) (2014) 1840.

[25] M. Saha, B. B. Dally, P. R. Medwell, A. Chinnici, Effect of particle size on the MILD combustion characteristics of pulverised brown coal, Fuel Process. Technol. 155 (2017) 74–87.

[26] M. Saha, B. B. Dally, P. R. Medwell, A. Chinnici, Burning characteristics of Victorian brown coal under MILD combustion conditions, Combust. Flame 172 (2016) 252–270.

[27] A. Cavaliere, M. de Joannon, Mild Combustion, Prog. Energ. Combust. 30 (4) (2004) 329–366.

[28] J. A. Wünning, J. G. Wünning, Flameless oxidation to reduce thermal no-formation, Prog. Energ. Combust. 23 (1) (1997) 81–94.

[29] T. Plessing, N. Peters, J. G. Wünning, Laseroptical investigation of highly preheated combustion with strong exhaust gas recirculation, Proc. Combust. Inst. 27 (2) (1998) 3197–3204.

[30] A. Chinnici, G. Nathan, B. Dally, An experimental study of the stability and performance characteristics of a Hybrid Solar Receiver Combustor operated in the MILD combustion regime, Proc. Combust. Inst. DOI: 10.1016/j.proci.2018.05.099.

[31] J. M. Beér, Minimizing $NO_x$ emissions from stationary combustion; reaction engineering methodology, Chem. Eng. Sci. 49 (24, Part A) (1994) 4067–4083.

[32] K. Döbbeling, J. Hellat, H. Koch, 25 Years of BBC/ABB/Alstom Lean Premix Combustion Technologies, J. Eng. Gas Turb. Power 1 (2007) 2–12.

[33] G. Sturgess, J. Zelina, D. T. Shouse, W. Roquemore, Emissions reduction technologies for military gas turbine engines, J. Propul. Power 21 (2) (2005) 193–217.

[34] M. J. Dunn, A. R. Masri, R. W. Bilger, A new piloted premixed jet burner to study strong finite-rate chemistry effects, Combust. Flame 151 (1-2) (2007) 46–60.

[35] M. J. Dunn, A. R. Masri, R. W. Bilger, R. S. Barlow, Finite Rate Chemistry Effects in Highly Sheared Turbulent Premixed Flames, Flow, Turbul. Combust. 85 (3) (2010) 621–648.

[36] A. Masri, R. Dibble, R. Barlow, The structure of turbulent nonpremixed flames revealed by Raman-Rayleigh-LIF measurements, Prog. Energy Combust. Sci. 22 (4) (1996) 307–362.

[37] J. Kent, Turbulent diffusion flame sooting—Relationship to smoke-point tests, Combust. Flame 67 (3) (1987) 223–233.

[38] R. V. Bandaru, S. R. Turns, Turbulent jet flames in a crossflow: effects of some jet, crossflow, and pilot-flame parameters on emissions, Combust. Flame 121 (1) (2000) 137 – 151.

[39] K. Lyle, L. Tseng, J. Gore, N. Laurendeau, A study of pollutant emission characteristics of partially premixed turbulent jet flames, Combust. Flame 116 (4) (1999) 627–639.

[40] S. Sarathy, A. Farooq, G. T. Kalghatgi, Recent progress in gasoline surrogate fuels, Prog. Energy Combust. Sci. 65 (2018) 67–108.

[41] Y. Zhang, K. P. Somers, M. Mehl, W. J. Pitz, R. F. Cracknell, H. J. Curran, Probing the antagonistic effect of toluene as a component in surrogate fuel models at low temperatures and high pressures. A case study of toluene/dimethyl ether mixtures, Proc. Combust. Inst. 36 (1) (2017) 413–421.

[42] J. Herzler, M. Fikri, K. Hitzbleck, R. Starke, C. Schulz, P. Roth, G. Kalghatgi, Shock-tube study of the autoignition of n-heptane/toluene/air mixtures at intermediate temperatures and high pressures, Combust. Flame 149 (1) (2007) 25–31.

[43] G. Kukkadapu, K. Kumar, C.-J. Sung, M. Mehl, W. J. Pitz, Experimental and surrogate modeling study of gasoline ignition in a rapid compression machine, Combust. Flame 159 (10) (2012) 3066–3078.

[44] G. Kukkadapu, K. Kumar, C.-J. Sung, M. Mehl, W. J. Pitz, Autoignition of gasoline surrogates at low temperature combustion conditions, Combust. Flame 162 (5) (2015) 2272–2285.

[45] C. Westbrook, W. Pitz, M. Mehl, H. Curran, Detailed chemical kinetic reaction mechanisms for primary reference fuels for diesel cetane number and spark-ignition octane number, Proc. Combust. Inst. 33 (1) (2011) 185–192.

[46] M. Mehl, W. J. Pitz, C. K. Westbrook, H. J. Curran, Kinetic modeling of gasoline surrogate components and mixtures under engine conditions, Proc. Combust. Inst. 33 (1) (2011) 193–200.

[47] L. Cai, H. Pitsch, Optimized chemical mechanism for combustion of gasoline surrogate fuels, Combust. Flame 162 (5) (2015) 1623–1637.

[48] J. Ye, P. R. Medwell, E. Varea, S. Kruse, B. B. Dally, H. G. Pitsch, An experimental study on MILD combustion of prevaporised liquid fuels, Appl. Energ. 151 (2015) 93–101.

[49] M. J. Evans, J. A. Sidey, J. Ye, P. R. Medwell, B. B. Dally, E. Mastorakos, Temperature and Reaction Zone Imaging in Turbulent Swirling Dual-Fuel Flames, Proc. Combust. Inst. DOI: 10.1016/j.proci.2018.07.076.

[50] B. Gauthier, D. Davidson, R. Hanson, Shock tube determination of ignition delay times in full-blend and surrogate fuel mixtures, Combust. Flame 139 (4) (2004) 300–311.

[51] T. Lu, C. K. Law, Linear time reduction of large kinetic mechanisms with directed relation graph: n-Heptane and iso-octane, Combust. Flame 144 (1) (2006) 24–36.

[52] S. Kruse, J. Ye, Z. Sun, A. Attili, B. B. Dally, P. R. Medwell, H. Pitsch, Experimental investigation of soot evolution in a turbulent non-premixed prevaporized toluene flame, Proc. Combust. Inst. DOI: 10.1016/j.proci.2018.05.075.

[53] Q. N. Chan, P. R. Medwell, B. B. Dally, Z. T. Alwahabi, G. J. Nathan, New Seeding Methodology

for Gas Concentration Measurements, Appl. Spectrosc. 66 (7) (2012) 803–809.

[54] P. R. Medwell, Q. N. Chan, B. B. Dally, S. Mahmoud, Z. T. Alwahabi, G. J. Nathan, Temperature measurements in turbulent non-premixed flames by two-line atomic fluorescence, Proc. Combust. Inst. 34 (2) (2013) 3619–3627.

[55] D. Gu, Z. Sun, B. B. Dally, P. R. Medwell, Z. T. Alwahabi, G. J. Nathan, Simultaneous measurements of gas temperature, soot volume fraction and primary particle diameter in a sooting lifted turbulent ethylene/air non-premixed flame, Combust. Flame 179 (2017) 33–50.

[56] P. R. Medwell, P. A. M. Kalt, B. B. Dally, Reaction Zone Weakening Effects under Hot and Diluted Oxidant Stream Conditions, Combust. Sci. Technol. 181 (7) (2009) 937–953.

[57] P. R. Medwell, Q. N. Chan, P. A. M. Kalt, Z. T. Alwahabi, B. B. Dally, G. J. Nathan, Instantaneous Temperature Imaging of Diffusion Flames Using Two-Line Atomic Fluorescence, Appl. Spectrosc. 64 (2) (2010) 173–176.

[58] Q. N. Chan, P. R. Medwell, P. A. Kalt, Z. T. Alwahabi, B. B. Dally, G. J. Nathan, Simultaneous imaging of temperature and soot volume fraction, Proc. Combust. Inst. 33 (1) (2011) 791–798.

[59] B. Quay, T.-W. Lee, T. Ni, R. Santoro, Spatially resolved measurements of soot volume fraction using laser-induced incandescence, Combust. Flame 97 (3) (1994) 384–392.

[60] C. R. Shaddix, K. C. Smyth, Laser-induced incandescence measurements of soot production in steady and flickering methane, propane, and ethylene diffusion flames, Combust. Flame 107 (4) (1996) 418–452.

[61] N. Qamar, Z. Alwahabi, Q. Chan, G. Nathan, D. Roekaerts, K. King, Soot volume fraction in a piloted turbulent jet non-premixed flame of natural gas, Combust. Flame 156 (7) (2009) 1339–1347.

[62] Z. Sun, D. Gu, G. Nathan, Z. Alwahabi, B. Dally, Single-shot, Time-Resolved planar Laser-Induced Incandescence (TiRe-LII) for soot primary particle sizing in flames, Proc. Combust. Inst. 35 (3) (2015) 3673–3680.

[63] K. K. Foo, Z. Sun, P. R. Medwell, Z. T. Alwahabi, B. B. Dally, G. J. Nathan, Experimental investigation of acoustic forcing on temperature, soot volume fraction and primary particle diameter in non-premixed laminar flames, Combust. Flame 181 (2017) 270–282.

[64] D. Gu, Z. Sun, G. J. Nathan, P. R. Medwell, Z. T. Alwahabi, B. B. Dally, Improvement of precision and accuracy of temperature imaging in sooting flames using two-line atomic fluorescence (TLAF), Combust. Flame 167 (2016) 481–493.

[65] P. R. Medwell, Q. N. Chan, B. B. Dally, Z. T. Alwahabi, S. Mahmoud, G. F. Metha, G. J. Nathan, Flow seeding with elemental metal species via an optical method, Appl. Phys. B 107 (3) (2012) 665–668.

[66] D. H. Gu, Z. W. Sun, P. R. Medwell, Z. T. Alwahabi, B. B. Dally, G. J. Nathan, Mechanism for laser-induced fluorescence signal generation in a nanoparticle-seeded flow for planar flame thermometry,

Appl. Phys. B 118 (2) (2015) 209–218.

[67] S. R. Shabanian, P. R. Medwell, M. Rahimi, A. Frassoldati, A. Cuoci, Kinetic and fluid dynamic modeling of ethylene jet flames in diluted and heated oxidant stream combustion conditions, Appl. Therm. Eng. 52 (2013) 538–554.

[68] H. Curran, P. Gaffuri, W. Pitz, C. Westbrook, A comprehensive modeling study of iso-octane oxidation, Combust. Flame 129 (3) (2002) 253–280.

[69] A. Attili, F. Bisetti, M. E. Mueller, H. Pitsch, Formation, growth, and transport of soot in a three-dimensional turbulent non-premixed jet flame, Combust. Flame 161 (7) (2014) 1849–1865.

[70] R. Minetti, M. Carlier, M. Ribaucour, E. Therssen, L. Sochet, A rapid compression machine investigation of oxidation and auto-ignition of n-Heptane: Measurements and modeling, Combust. Flame 102 (3) (1995) 298–309.

[71] K. Fieweger, R. Blumenthal, G. Adomeit, Self-ignition of S.I. engine model fuels: A shock tube investigation at high pressure, Combust. Flame 109 (4) (1997) 599–619.

[72] Y. Huang, C. Sung, J. Eng, Laminar flame speeds of primary reference fuels and reformer gas mixtures, Combust. Flame 139 (3) (2004) 239–251.

[73] S. Jerzembeck, N. Peters, P. Pepiot-Desjardins, H. Pitsch, Laminar burning velocities at high pressure for primary reference fuels and gasoline: Experimental and numerical investigation, Combust. Flame 156 (2) (2009) 292–301.

[74] H. Ciezki, G. Adomeit, Shock-tube investigation of self-ignition of n-heptane-air mixtures under engine relevant conditions, Combust. Flame 93 (4) (1993) 421–433.

[75] L. Cancino, M. Fikri, A. Oliveira, C. Schulz, Autoignition of gasoline surrogate mixtures at intermediate temperatures and high pressures: Experimental and numerical approaches, Proc. Combust. Inst. 32 (1) (2009) 501–508.

[76] P. Dirrenberger, P. Glaude, R. Bounaceur, H. L. Gall, A. P. da Cruz, A. Konnov, F. Battin-Leclerc, Laminar burning velocity of gasolines with addition of ethanol, Fuel 115 (2014) 162–169.

[77] M. Fikri, J. Herzler, R. Starke, C. Schulz, P. Roth, G. Kalghatgi, Autoignition of gasoline surrogates mixtures at intermediate temperatures and high pressures, Combust. Flame 152 (1) (2008) 276–281.

[78] M. Hartmann, I. Gushterova, M. Fikri, C. Schulz, R. Schießl, U. Maas, Auto-ignition of toluene-doped n-heptane and iso-octane/air mixtures: High-pressure shock-tube experiments and kinetics modeling, Combust. Flame 158 (1) (2011) 172 – 178.

[79] D. Bradley, R. Hicks, M. Lawes, C. Sheppard, R. Woolley, The Measurement of Laminar Burning Velocities and Markstein Numbers for Iso-octane–Air and Iso-octane–n-Heptane–Air Mixtures at Elevated Temperatures and Pressures in an Explosion Bomb, Combust. Flame 115 (1) (1998) 126–144.

[80] P. Dagaut, M. Reuillon, M. Cathonnet, High Pressure Oxidation of Liquid Fuels from Low to High

Temperature. 2. Mixtures of n-Heptane and iso-Octane, Combust. Sci. Technol. 103 (1-6) (1994) 315–336.

[81] M. Ihme, Y. C. See, Prediction of autoignition in a lifted methane/air flame using an unsteady flamelet/progress variable model, Combust. Flame 157 (10) (2010) 1850–1862.

[82] J. Luo, M. Yao, H. Liu, B. Yang, Experimental and numerical study on suitable diesel fuel surrogates in low temperature combustion conditions, Fuel 97 (2012) 621–629.

[83] M. J. Evans, P. R. Medwell, Z. F. Tian, A. Frassoldati, A. Cuoci, A. Stagni, Ignition Characteristics in Spatially Zero-, One- and Two-Dimensional Laminar Ethylene Flames, AIAA J. 54 (10) (2016) 3255–3264.

[84] P. R. Medwell, M. J. Evans, Q. N. Chan, V. R. Katta, Laminar flame calculations for analysing trends in autoignitive jet flames in a hot and vitiated coflow, Energy Fuels 30 (10) (2016) 8680–8690.

[85] M. de Joannon, P. Sabia, G. Cozzolino, G. Sorrentino, A. Cavaliere, Pyrolitic and Oxidative Structures in Hot Oxidant Diluted Oxidant (HODO) MILD Combustion, Combust. Sci. Technol. 184 (7-8) (2012) 1207–1218.

[86] J. A. Sidey, E. Mastorakos, Simulations of laminar non-premixed flames of methane with hot combustion products as oxidiser, Combust. Flame 163 (2016) 1–11.

[87] M. J. Evans, P. R. Medwell, Z. F. Tian, J. Ye, A. Frassoldati, A. Cuoci, Effects of oxidant stream composition on non-premixed laminar flames with heated and diluted coflows, Combust. Flame 178 (2017) 297–310.

[88] M. J. Evans, A. Chinnici, P. R. Medwell, J. Ye, Ignition features of methane and ethylene fuel-blends in hot and diluted coflows, Fuel 203 (2017) 279–289.

[89] M. Ihme, Y. C. See, LES flamelet modeling of a three-stream MILD combustor: Analysis of flame sensitivity to scalar inflow conditions, Proc. Combust. Inst. 33 (2011) 1309–1217.

[90] M. J. Evans, C. Petre, P. R. Medwell, A. Parente, Generalisation of the Eddy-Dissipation Concept for Jet Flames with Low Turbulence and Low Damköhler Number, Proc. Combust. Inst. DOI: 10.1016/j.proci.2018.06.017.

[91] P. Sabia, G. Sorrentino, A. Chinnici, A. Cavaliere, R. Ragucci, Dynamic Behaviors in Methane MILD and Oxy-Fuel Combustion. Chemical Effect of $CO_2$, Energy Fuels 29 (3) (2015) 1978–1986.

[92] P. Sabia, M. L. Lavadera, P. Giudicianni, G. Sorrentino, R. Ragucci, M. de Joannon, $CO_2$ and $H_2O$ effect on propane auto-ignition delay times under mild combustion operative conditions, Combust. Flame 162 (3) (2015) 533–543.

[93] P. Sabia, M. Lubrano Lavadera, G. Sorrentino, P. Giudicianni, R. Ragucci, M. de Joannon, $H_2O$ and $CO_2$ Dilution in MILD Combustion of Simple Hydrocarbons, Flow, Turbul. Combust. 96 (2) (2016) 433–448.

[94] Y. Tu, K. Su, H. Liu, S. Chen, Z. Liu, C. Zheng, Physical and chemical effects of $CO_2$ addition on $CH_4/H_2$ flames on a Jet in Hot Coflow (JHC) burner, Energy Fuels 30 (2) (2016) 1390–1399.

[95] C. Dai, B. Wang, Z. Shu, J. Mi, Thermal Characteristics of a CH4 Jet Flame in Hot Oxidant Stream: Dilution Effects of $CO_2$ and $H_2O$, Energy Fuels 32 (7) (2018) 7943–7958.

[96] J. Nygren, J. Engström, J. Walewski, C. F. Kaminski, M. Aldén, Applications and evaluation of two-line atomic LIF thermometry in sooting combustion environments, Meas. Sci. Technol. 12 (8) (2001) 1294.

[97] A. D'Anna, M. Alf, B. Apicella, A. Tregrossi, A. Ciajolo, Effect of Fuel/Air Ratio and Aromaticity on Sooting Behavior of Premixed Heptane Flames, Energy Fuels 21 (5) (2007) 2655–2662.

[98] K. Narayanaswamy, G. Blanquart, H. Pitsch, A consistent chemical mechanism for oxidation of substituted aromatic species, Combust. Flame 157 (10) (2010) 1879–1898.

[99] F. Liu, H. Guo, G. J. Smallwood, Ö. L. Gülder, Effects of gas and soot radiation on soot formation in a coflow laminar ethylene diffusion flame, J. Quant. Spectrosc. Radiat. Transfer 73 (2) (2002) 409–421.

[100] V. R. Katta, S. K. Aggarwal, W. M. Roquemore, Evaluation of chemical-kinetics models for n-heptane combustion using a multidimensional CFD code, Fuel 93 (2012) 339–350.

[101] F. Liu, H. Guo, G. J. Smallwood, Effects of radiation model on the modeling of a laminar coflow methane/air diffusion flame, Combust. Flame 138 (1) (2004) 136–154.

[102] P. Coelho, O. Teerling, D. Roekaerts, Spectral radiative effects and turbulence/radiation interaction in a non-luminous turbulent jet diffusion flame, Combust. Flame 133 (1) (2003) 75–91.

[103] P. Coelho, Numerical simulation of the interaction between turbulence and radiation in reactive flows, Prog. Energy Combust. Sci. 33 (4) (2007) 311–383.

[104] M. Frenklach, H. Wang, Detailed modeling of soot particle nucleation and growth, Proc. Combust. Inst. 23 (1) (1991) 1559–1566.

[105] F. Wang, J. Mi, P. Li, Combustion Regimes of a Jet Diffusion Flame in Hot Co-flow, Energy Fuels 27 (6) (2013) 3488–3498.

[106] M. de Joannon, G. Sorrentino, A. Cavaliere, MILD combustion in diffusion-controlled regimes of Hot Diluted Fuel, Combust. Flame 159 (2012) 1832–1839.

[107] K.-P. Cheong, G. Wang, J. Mi, B. Wang, R. Zhu, W. Ren, Premixed MILD Combustion of Propane in a Cylindrical Furnace with a Single Jet Burner: Combustion and Emission Characteristics, Energy Fuels 32 (8) (2018) 8817–8829.

[108] P. Sabia, M. de Joannon, A. Picarelli, A. Chinnici, R. Ragucci, Modeling Negative Temperature Coefficient region in methane oxidation, Fuel 91 (1) (2012) 238–245.

## List of Figures

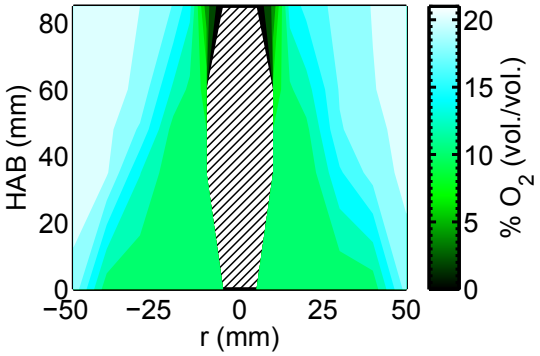


(a) $O_2$

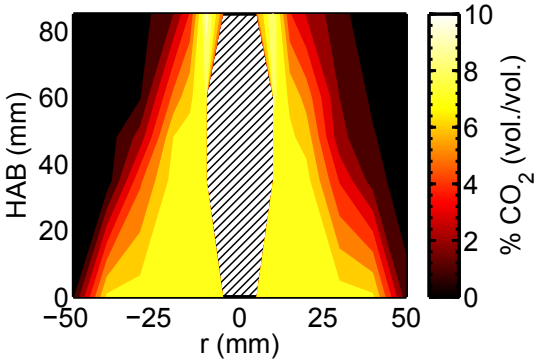


(b) $CO_2$

Fig. 1: Measured volumetric concentrations of $O_2$ and $CO_2$ (dry basis), for HEP-2, at the centre plane region at different heights above the burner jet exit plane (HAB).

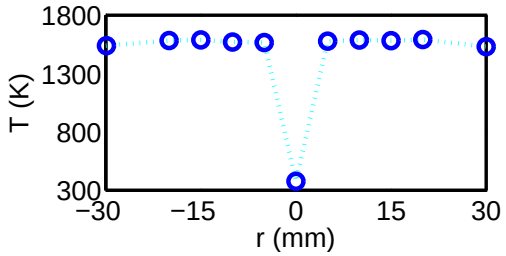


Fig. 2: Mean radial profile of measured coflow temperature, for HEP-2, at the jet exit plane.

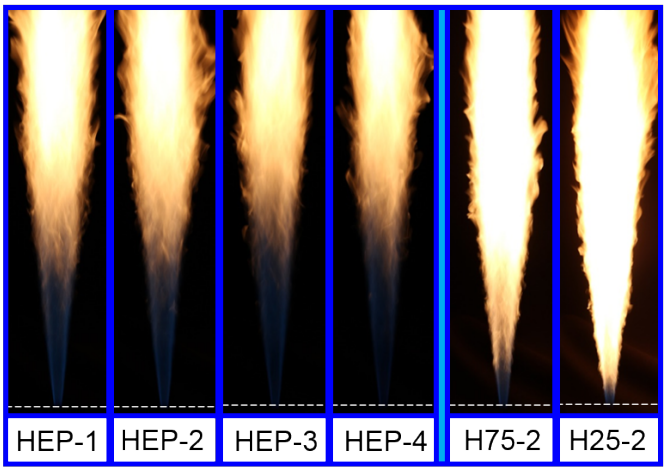


Fig. 3: Photographs of flames with increasing toluene concentration. From left-to-right: pure $n$-heptane, 25% toluene, 75% toluene. Photographs are 100 mm wide, and approximately 375 mm high, with the jet exit plane at the bottom of each image. Photographs were taken through a 50 mm lens at f/8 and ISO-100 with exposure times of 1/15 s. The white dashed lines in each image show the flame lift-off heights.

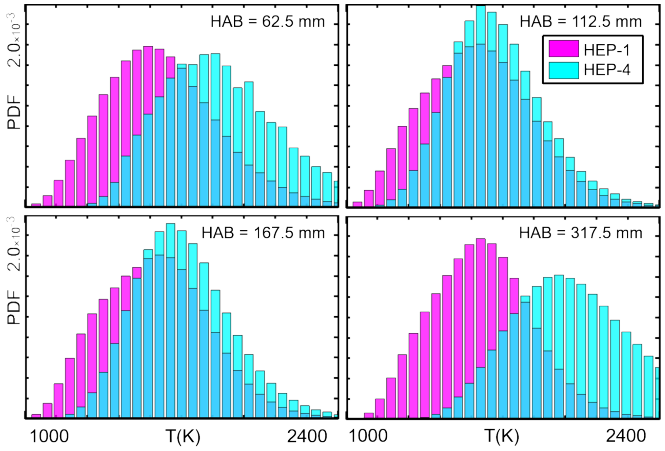


Fig. 4: Probability distributions of temperatures for cases HEP-1 and 4 centred at four different heights above the jet exit plane. Data taken from a strip approximately 2 mm tall, with bins of 50 K, from 500 images.

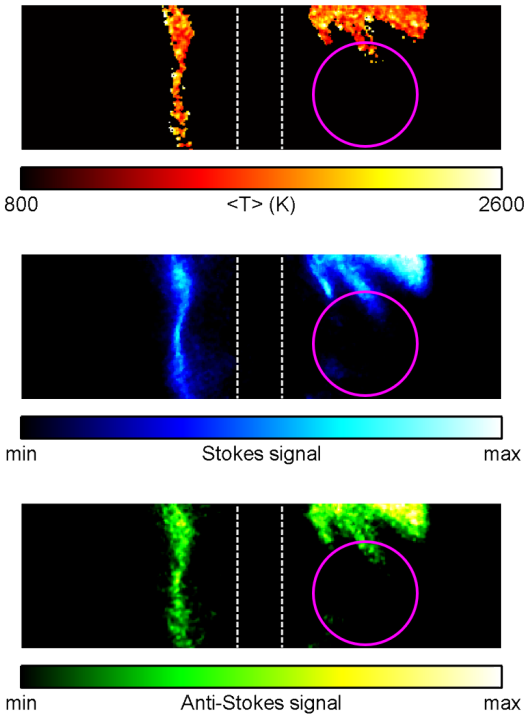


Fig. 5: Instantaneous temperature and field, Stokes signal and Anti-Stokes signal in HEP-4 centred 110 mm above the jet exit plane with a break in the flame circled. Imaging area is 15 mm × 50 mm, and white lines represent the I.D. of the central fuel jet.

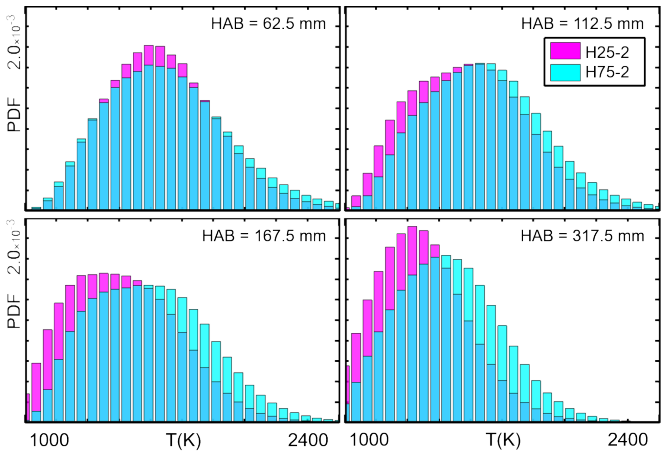


Fig. 6: Probability distributions of temperatures for the H25-2 and H75-2 flames, centred at four different heights above the jet exit plane. Data taken from a strip approximately 2 mm tall, with bins of 50 K, from 500 images.

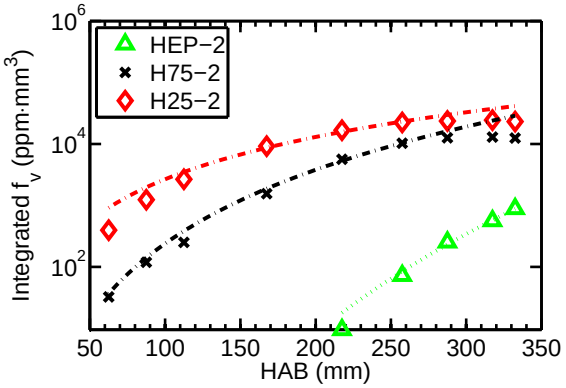


Fig. 7: Integrated soot volume fraction, for three $n$-heptane/toluene flames at different heights above the jet exit plane. Data averaged over a strip approximately 2 mm tall. Curves show best fit of a power law for each flame. Curve fits for Cases H25-2 and H75-2 only used data within 250 mm of the jet exit plane.

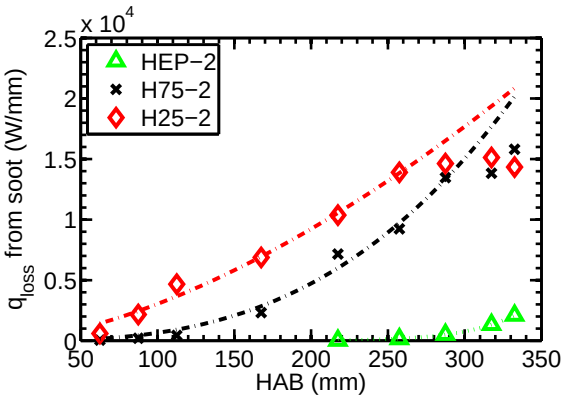


Fig. 8: Calculated radiative heat loss from soot in $n$-heptane/toluene flames based on measurable SVF from LII and modal measured temperature from NTLAF. Curves show best fit of a power law for each flame. Curve fits for Cases H25-2 and H75-2 only used data within 250 mm of the jet exit plane.

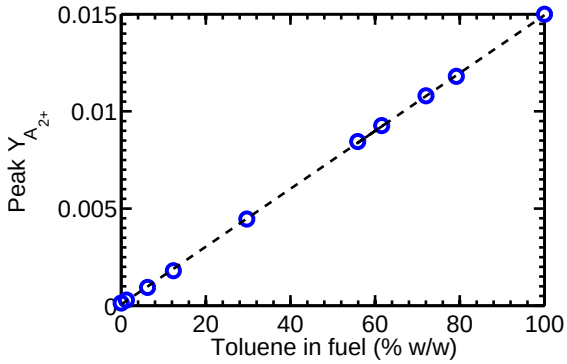


Fig. 9: Peak total $Y_{A_{2+}}$ in simulated $n$-heptane/toluene opposed-flow flames with different concentrations of toluene, with dashed line showing linear regression ($R^2 = 0.9999$). Oxidant composition from cases HEP-2, H25-2 and H75-2 are found in Table 1.

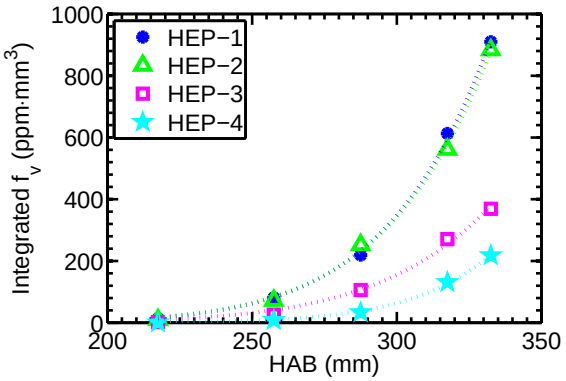


Fig. 10: Integrated soot volume fraction, for four $n$-heptane flames in different coflow conditions and various heights above the jet exit plane. Data averaged over a strip approximately 2 mm tall. Curves show best fit of a power law for each flame.

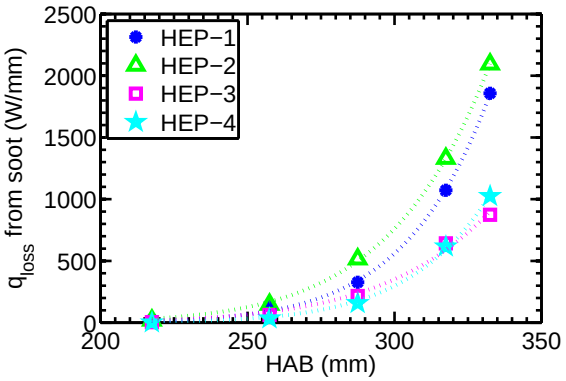


Fig. 11: Calculated radiative heat loss from $n$-heptane flames in different coflows based on measurable SVF from LII and modal measured temperature from NTLAF. Curves show best fit of a power law for each flame.

## List of Tables

Table 1: Summary of the jet fuel (ratios by liquid volume) and coflow (wet basis) streams.

| Case | Fuel | $X_{O_2}$ | $X_{CO_2}$ | $X_{H_2O}$ | $T_{cofl}$ (K) |
|---|---|---|---|---|---|
| HEP-1 | *n*-heptane | 0.108 | 0.063 | 0.063 | 1490 |
| HEP-2 | *n*-heptane | 0.096 | 0.070 | 0.070 | 1590 |
| HEP-3 | *n*-heptane | 0.085 | 0.077 | 0.077 | 1590 |
| HEP-4 | *n*-heptane | 0.075 | 0.061 | 0.121 | 1520 |
| H75-2 | 3:1 *n*-heptane/toluene | 0.096 | 0.070 | 0.070 | 1590 |
| H25-2 | 1:3 *n*-heptane/toluene | 0.096 | 0.070 | 0.070 | 1590 |

Table 2: Summary of flame characteristics in the four $n$-heptane only flame cases. Most probable temperatures are provided based on 50 K bins, representative of the accuracy of the measurements.

| Case | Mean lift-off height (mm) | Most probable temperature (K) | | | |
|---|---|---|---|---|---|
| | | 62.5 mm | 112.5 mm | 167.5 mm | 317.5 mm |
| HEP-1 | 9.3 | 1550 | 1600 | 1600 | 1600 |
| HEP-2 | 9.3 | 1600 | 1700 | 1700 | 1700 |
| HEP-3 | 10.0 | 1550 | 1650 | 1700 | 1700 |
| HEP-4 | 10.7 | 1850 | 1600 | 1650 | 1950 |

Table 3: Percentage of images with ruptured flame fronts in two cases, centred at three different heights.

| Case | Percentage of images (%) | | |
|---|---|---|---|
| | 60 mm | 110 mm | 165 mm |
| HEP-1 | 0 | 11 | 3 |
| HEP-4 | 0 | 24 | 7 |

Table 4: Summary of flame characteristics in the $n$-heptane/toluene flame cases. Most probable temperatures are provided based on 50 K bins, representative of the accuracy of the measurements.

| Case | Mean lift-off height (mm) | Most probable temperature (K) | | | |
|---|---|---|---|---|---|
| | | 62.5 mm | 112.5 mm | 167.5 mm | 317.5 mm |
| HEP-2 | 9.3 | 1600 | 1650 | 1700 | 1700 |
| H75-2 | 10.1 | 1550 | 1600 | 1550 | 1450 |
| H25-2 | 11.3 | 1550 | 1600 | 1350 | 1300 |

Table 5: Mean heat loss (mW/mm) from radiant gases in $n$-heptane and $n$-heptane/toluene flames.

| Case | Mean $q_{loss}$ from gas phase (mW/mm) |
|---|---|
| HEP-1 | 1.81 |
| HEP-2 | 2.42 |
| HEP-3 | 2.37 |
| HEP-4 | 3.18 |
| H75-2 | 1.67 |
| H25-2 | 1.29 |

Table 6: Peak total mass fraction of polycyclic hydrocarbons ($Y_{A_{2+}}$) and minimum net heat release rate (HRR) in simulated *n*-heptane opposed-flow flames. Oxidant details given in Table 1.

| Case | Peak $Y_{A_{2+}} \times 10^{-4}$ | Min. HRR (W/mm$^3$) |
|---|---|---|
| HEP-1 | 1.20 | -68.2 |
| HEP-2 | 1.33 | -68.3 |
| HEP-3 | 0.94 | -60.3 |
| HEP-4 | 0.45 | -48.4 |

**Supplementary Material**

**Click here to download Supplementary Material: CNF-D-18-00755R1-SuppData-v01.pdf**